CrystEngComm

Facile Synthesis of Highly Luminescent Lithium Silicate Nanocrystals with Varying Crystal Structure and Morphology

Journal:	*CrystEngComm*
Manuscript ID	CE-ART-12-2018-002120.R1
Article Type:	Paper
Date Submitted by the Author:	03-Feb-2019
Complete List of Authors:	Eladgham, Ebtesam ; Virginia Commonwealth University College of Humanities and Sciences, Department of Chemistry Demchenko, Denis ; Virginia Commonwealth University, Department of Physics Nakagawara, Tanner ; Virginia Commonwealth University, Department of Electrical and Computer Engineering Ozgur, U.; Virginia Commonwealth University, Department of Electrical and Computer Engineering Arachchige, Indika; Viginia Commonwealth University, Chemistry

Facile Synthesis of Highly Luminescent Lithium Silicate Nanocrystals with Varying Crystal Structure and Morphology

*Ebtesam H. Eladgham,[1,2] Denis O. Demchenko,[3] Tanner A. Nakagawara,[4] Ümit Özgür,[4] and Indika U. Arachchige[1]**

[1]Department of Chemistry, Virginia Commonwealth University, Richmond, Virginia 23284, United States

[2]Department of Solar Energy, National Research Center, Dokki, Cairo 12622, Egypt

[3]Department of Physics, Virginia Commonwealth University, Richmond, Virginia 23284, United States

[4]Department of Electrical and Computer Engineering, Virginia Commonwealth University, Richmond, Virginia 23284, United States

ABSTRACT

Lithium silicates have received noteworthy interest as a class of materials with significant potential in lithium ion batteries, ionic conductors, optical waveguides and sensors, and efficient sorbents for CO_2 capture. Herein we report the optical properties, electronic structures, and surface characteristics of two distinct lithium silicate crystal phases using first-principles hybrid density functional theory (DFT) calculations and in-depth experimental characterization studies. Orthorhombic Li_2SiO_3 (space group *Cmc21*) and $Li_2Si_2O_5$ (space group *Ccc2*) nanoparticles (NPs) passivated with alkylamine and alkane surface functionalities were produced by reaction of SiI_4 with n-butyllithium in the presence of 1,2-hexadecanediol. As-synthesized nanostructures exhibit poor crystallinity, which upon annealing at 600 ºC adopt phase-pure orthorhombic crystal structures with spherical (Li_2SiO_3), polyhedral or rod-shaped ($Li_2Si_2O_5$) morphologies. Surface analysis of Li_2SiO_3 and $Li_2Si_2O_5$ NPs reveals distinct chemical states for Li^+, Si^{n+}, and O^{n-}, consistent with their stoichiometry and higher binding energies for constituent elements in $Li_2Si_2O_5$ NPs. Hybrid functional calculations predict indirect and direct energy gaps of 7.79 and 7.80 eV for Li_2SiO_3 and $Li_2Si_2O_5$, respectively signifying the insulating nature of extended solids. Nonetheless, as-synthesized Li_2SiO_3 and $Li_2Si_2O_5$ NPs exhibit high intensity visible photoluminescence (quantum yields = 10−30%) with nanosecond timescale decays at 15 K and 295 K, which we attribute to radiative recombination from surface/interface traps. The facile colloidal synthesis provides control over crystal structure and composition of nanostructured lithium silicates, which will potentially widen their applications as visible to IR transparent optical materials, chromophores, waveguides, sensors, and high surface area CO_2 sorbents.

INTRODUCTION

Silicates show a variety of stoichiometries and crystal structures that are naturally abundant. They form most of earth's crust and other structures in solar system including terrestrial planets, rocky moons, and asteroids.[1] Lithium silicates are an important sub-class of the silicate family with potential applications in many technologies. These include but are not limited to lithium ion batteries,[2] ionic conductors,[3, 4] visible to IR transparent optical materials,[5] waveguides,[6] sensors,[7] and high temperature sorbents for efficient CO_2 capture.[8, 9]

Orthorhombic Li_2SiO_3 and $Li_2Si_2O_5$ show noteworthy interest as solid electrolytes and high capacity cathode materials for lithium ion batteries.[2-4] Amorphous thin films of Li_2SiO_3 exhibit limited ionic conductivity at 298 K, which increases by up to two orders of magnitude at higher temperatures (500-700 K) compared to polycrystalline Li_2SiO_3.[3, 4] Likewise, recent reports on 2-D and 3-D micro-/nano-structures and nanowires of $Li_2Si_2O_5$ suggest high initial Li ion storage capacity than commercial Li-Mn-O and Li-Co-O cathode materials.[10, 11] Among SiO_2/Li cells reported, reversible conversion reaction of SiO_2 into $Li_2Si_2O_5$ results in reduction of charge capacity by only <0.01% during the first 100 cycles,[12] making $Li_2Si_2O_5$ an attractive material for durable and high capacity charge storage device applications.

Optical properties of lithium silicates are known and categorized as insulators. Despite their insulating nature, both Li_2SiO_3 and $Li_2Si_2O_5$ exhibit intense visible (blue) absorption and photoluminescence (PL) that can be attributed to surface defects. Such optical activity has been wrongfully assumed to originate from quantum-confined Si nanoparticles (NPs) with diamond cubic and BC8 structure types.[13-17] On the theoretical side, studies on electronic structure and energy gaps of lithium silicates are limited. For instance, electronic structure calculated by the density functional theory (DFT) using the Perdew-Burke-Ernzerhof (PBE)[18] parametrization of the generalized gradient approximation (GGA) predicts indirect bandgaps of 4.575 and 4.776 eV

for Li_2SiO_3 and $Li_2Si_2O_5$, respectively.[19] In contrast, larger bandgaps of 5.7 eV for Li_2SiO_3 and 5.5 eV for $Li_2Si_2O_5$ were calculated by using the Perdew-Wang 91[20] GGA approximation to the DFT.[21] On the contrary, linear combination of atomic orbitals (LCAO) calculations report bandgaps as high as 7.26 and 7.45 eV, respectively.[22] It is expected that GGA approximations to the DFT will significantly underestimate the values of energy gaps. On the other hand, semi-empirical nature of the LCAO method can lead to varying results, depending on the input parameters. Thus, the electronic structure and optical properties of lithium silicates remain uncertain, despite their potential as (nano)phosphors in a number of new technologies.

Over the past two decades, lithium silicate bulk and micron-sized crystals were produced by physical techniques such as laser ablation and ball milling[23] and chemical routes that include solid state synthesis,[6, 7] atomic layer deposition,[3, 11] sol-gel chemistry[9, 24] and hydrothermal or solvothermal reactions.[19, 25, 26] These methods yield poor structural and morphological control and often result in large (1-2 μm) irregular-shaped crystals, amorphous NPs, and/or mixed phases of Li_2SiO_3, $Li_2Si_2O_5$, Li_4SiO_4, and SiO_2. Moreover, the synthesis of nanostructured silicates via aforementioned methods imposes a great challenge as they often fail to offer narrow size distribution, desired homogeneity, and phase purity. In contrast, the use of colloidal synthesis would eliminate such drawbacks while providing better control over physical properties, as it places the ability to produce size-/composition-/shape-controlled crystals. However, to the best of our knowledge, the synthesis of phase pure Li_2SiO_3 and $Li_2Si_2O_5$ as discrete nanocrystals with varying morphology and composition has not been reported.

Herein, we report the first colloidal synthesis of lithium metasilicate and disilicate NPs via reaction of SiI_4 with n-butyllithium and 1,2 hexadecandiol in alkylamine/alkene solvents. As-synthesized NPs exhibit poor crystallinity, thus were transformed into orthorhombic Li_2SiO_3

(space group *Cmc21*) and $Li_2Si_2O_5$ (space group *Ccc2*) NPs with varying shapes via post-synthetic annealing at 600 ºC. The surface analysis of Li_2SiO_3 and $Li_2Si_2O_5$ NPs reveals distinct chemical states for Li^+, Si^{n+}, and O^{n-}, consistent with their stoichiometry and higher binding energies for constituent elements in the later NPs. Hybrid functional calculations predict indirect and direct energy gaps of 7.79 and 7.80 eV for bulk orthorhombic Li_2SiO_3 and $Li_2Si_2O_5$, respectively, whereas as-synthesized crystals exhibit high intensity visible PL with nanosecond timescale decays at 15 K and 295 K, which we attribute to emissive surface/interface traps. The colloidal synthesis developed in this study provides better control over size, composition, and crystal structure of discrete lithium silicates, specifically on the nanoscale, which will expand the library of highly luminescent nanophosphors beyond perovskites, lanthanides, and metal chalcogenide and pnictide nanostructures.[27-29]

EXPERIMENTAL SECTION

Materials. Silicon (IV) iodide (SiI_4, 99%) was purchased from Alfa Aesar. 1,2-Hexadecanediol (HDD, 98%) was purchased from TCI America. Oleylamine (OLA, 98%), n-butyllithium (n-BuLi, 1.6 M in hexane), and chloroform were purchased from Sigma-Aldrich. Toluene, acetone, and methanol of ACS grade were purchased from Fisher. Toluene was dried using sodium, distilled under nitrogen, and stored over molecular sieves. Methanol was dried over molecular sieves and distilled under nitrogen. Acetone and chloroform were dried over molecular sieves and degassed under high purity argon for 30 min. OLA was dried under vacuum at 120 °C for 1 h prior to use. All other chemicals were used as received.

Synthesis of Amorphous-to-Poorly Crystalline Lithium Silicate ($Li_2Si_xO_y$) NPs. In a typical synthesis of $Li_2Si_xO_y$ NPs, 1 mmol (0.536 g) of SiI_4 and 0.4 mmol (0.103 g) of HDD were

dissolved in 15 mL of OLA in a three-neck flask. This mixture was heated at 120 °C for 15 min under vacuum, flushed with high purity argon, and continuously heated to 170 °C to produce a homogeneous pale-yellow solution. After 10 min at 170 °C, 3.75 mmol (for Li_2SiO_3 NPs) or 2.25 mmol (for $Li_2Si_2O_5$ NPs) of n-BuLi was rapidly injected at which point the reaction became colorless. The resultant seed nuclei were grown at 250 °C for 30 min to produce a brown color solution of amorphous-to-poorly crystalline $Li_2Si_xO_y$ NPs. The reaction flask was then cooled to 100 °C using compressed air and ~5 mL of freshly distilled toluene was added. The crude reaction mixture was further cooled to ~40 °C using compressed air and transferred into a nitrogen glove box. Purification of silicate NPs was done under inert atmosphere with no exposure to air. The crude solution was transferred to a centrifuge tube inside a glove box and ~7 mL of acetone or methanol was added, followed by centrifugation at 4000 rpm to obtain a brown precipitate of $Li_2Si_xO_y$ NPs. The precipitated NPs were washed with toluene/(acetone or methanol) (1:2 v/v) 2−3 times and dispersed in $CHCl_3$.

Synthesis of Orthorhombic Li_2SiO_3 and $Li_2Si_2O_5$ NPs. As-synthesized NP powders were annealed at 600 ºC for 2 h in an argon flow furnace to produce orthorhombic lithium silicate NPs. The powder samples were loaded onto platinum pans inside a nitrogen glove box and immediately transferred into a closed tube furnace under high purity argon. The temperature was raised from 25 ºC to 600 ºC within ~10 min and the samples were annealed at 600 ºC for 2 h. The annealed samples were cooled to 50 °C within 2 h and stored in a nitrogen glove box.

Physical Characterization. Powder diffraction patterns of all samples were recorded using PANalytical powder X-ray diffractometer (XRD) equipped with a Cu Kα radiation. A Nicolet 670 FT−IR instrument equipped with a single-reflection diamond ATR was used to record the infrared (IR) spectra of all samples. X-ray photoelectron spectroscopy (XPS) spectra were

collected using a Thermofisher ESCALAB 250 instrument equipped with an Al Kα radiation, 0.10 eV step size, and 500 μm illumination area. Samples were prepared by pressing the NP powders onto indium foil purchased from Sigma-Aldrich. The holder was loaded inside the glove box and sealed to eliminate the exposure to air and directly mounted in the instrument. A Cary 6000i UV−vis−near IR spectrophotometer (Agilent Technologies) equipped with an internal diffuse reflectance (DRA-2500) attachment was used to record the reflectance spectra of $Li_2Si_xO_y$ NPs. First, diffuse reflectance (DRA) spectra of powder samples were recorded using $BaSO_4$ background and then converted to absorption using Kubelka-Munk function.[30] The energy gaps were obtained by extrapolating the first major absorption to the intersection point of the baseline. PL and photoluminescence excitation (PLE) spectra of NPs dispersed in $CHCl_3$ were recorded using a Cary Eclipse fluorescence spectrophotometer (Agilent Technologies). PL and time-resolved PL (TRPL) spectra of solid NP films (drop casted on sapphire substrates) were recorded using a frequency doubled Ti:sapphire laser (385 nm wavelength, 150 fs pulse width, 8 kHz to 80 MHz repetition rate). Measurements were performed at room temperature (295 K) and low temperature (15 K) by mounting the substrate on a closed cycle He cryostat. A liquid nitrogen-cooled charge coupled device (CCD) camera connected to a spectrometer was employed to collect the steady-state PL spectra and a Hamamatsu streak camera with 25 ps temporal resolution was used to analyze the PL transients. Transmission electron microscopy (TEM) images were recorded using a Zeiss Libra 120 microscope equipped with a Gatan ultrascan 4000 camera operating at 120 kV. High-resolution TEM (HRTEM) images were recorded using FEI model Titan 8300 microscope equipped with a Gatan 794 multiscan camera operating at 300 kV. Silicate NPs dispersed in $CHCl_3$ were drop-casted on carbon coated Cu grids and dried in ambient air prior to TEM analysis. The PL quantum yields (QYs) were

measured relative to a standard dye, quinine sulfate, following a literature method.[31] The optical densities of the dye and $Li_2Si_xO_y$ NPs dispersed in $CHCl_3$ were matched to 0.18 at the excitation energy (335 nm) and the PL QYs were calculated based on the percent ratio of the integrated emission spectra of NPs and the dye recorded under identical experimental conditions.

Computational Methods. Electronic structure of lithium silicates was calculated using hybrid density functional theory, which is beyond semi-local approximations. We used Vienna Ab-initio Simulation Package (VASP) code,[32] with the projector augmented wave (PAW) pseudopotentials[33] and plane wave energy cutoffs of 500 eV. The structural relaxations of Li_2SiO_3 and $Li_2Si_2O_5$ were performed using PBE parameterization of the GGA approximation[34] to the DFT. Atomic coordinates and lattice constants were relaxed to minimize the forces to 0.01 eV/Å or less. Γ-point centered k-point grids of 4×2×5 and 4×1×5 were used for Li_2SiO_3 and $Li_2Si_2O_5$ lattices, respectively. While PBE produces satisfactory values for lattice parameters, the computed energy gaps are significantly underestimated for wide bandgap semiconductors and insulators. Here we obtain PBE bandgaps as 5.13 eV (Γ-Z indirect) and 5.22 eV (Γ-point direct) for Li_2SiO_3 and $Li_2Si_2O_5$, respectively in agreement with previous calculations.[8, 19, 21] In contrast, Heyd-Scuseria-Ernzerhof (HSE) hybrid functional[35] yields significantly more accurate bandgaps across a wide range of materials.[36] Thus, in this work the band structures of Li_2SiO_3 and $Li_2Si_2O_5$ were calculated using HSE with the fraction of exact exchange adjusted to 0.375, keeping the exchange range separation parameter at a typical 0.2 $Å^{-1}$. As previously shown[37, 38] this parametrization of HSE reproduces the low temperature bandgaps of oxide alloys in agreement with experiments. To directly compare optical properties from experiments and theory, absorption spectra of Li_2SiO_3 and $Li_2Si_2O_5$ were calculated using time-dependent hybrid functional theory (TD-HSE), as described in Paier et al.,[39] based on above exchange-tuned hybrid

HSE functional. In the TD-HSE calculations, the excitonic effects are approximately described by replacing the electron-hole ladder diagrams with the screened exchange. The dielectric function is obtained by solving the Casida's equation.[40] It has been reported that this is essentially equivalent to the Bethe-Salpeter equation, with the screened interaction (*W*) replaced with one-quarter of the nonlocal screened exchange term obtained from the standard or exchange tuned HSE.[39]

RESULTS AND DISCUSSION

When a mixture of SiI_4/OLA/HDD is heated above 120 °C, it progressively dissolves the SiI_4 powder and produces a homogeneous pale-yellow solution, consistent with the formation of Si^{4+}/amine and Si^{4+}/hydroxyl species.[41] Upon injection of n-BuLi at 170 °C, the reaction turned colorless suggesting the production of $Li_2Si_xO_y$ seeds. With further heating to 250 °C, an orange-brown product is formed, which we attribute to amorphous-to-poorly crystalline $Li_2Si_xO_y$ NPs. This is in sharp contrast to the reported syntheses of cubic Ge NPs, where $Ge^{4+/2+}$ precursors dispersed in OLA are typically reduced to $Ge^{(0)}$ by n-BuLi with no Li incorporation.[42-45] This drastic difference in chemistry can be attributed to more covalent character of Si^{4+} than $Ge^{4+/2+}$, which prefers compound formation with smaller Li^+ ions.[46] The use of n-BuLi as a surface passivating agent for Si NPs has been known for several years.[47-49] On the contrary, the direct reaction of n-BuLi with Si^{n+}/hydroxyl (or silanol-like) complexes has been reported by Gilman *et al.,*[50] where Li^+ would bond to the oxygen of the Si-O group producing lithium silanolate (Si-O-Li) species. Although the syntheses were performed under inert atmosphere, use of HDD as a potential surfactant ligand likely prompted the growth of $Li_2Si_xO_y$ seeds and NPs.

Powder X-ray diffraction patterns of as-synthesized $Li_2Si_xO_y$ NPs are either amorphous or poor crystalline where no Bragg reflections corresponding to any known crystal phases of

lithium silicates were noted (Supporting Information, Figure S1). Upon annealing $Li_2Si_xO_y$ NPs at 600 ºC, either orthorhombic Li_2SiO_3, orthorhombic $Li_2Si_2O_5$, or a mixture of phases were obtained depending on the synthesis. The production of different crystal phases with varying stoichiometry is governed by the molar ratio of SiI_4: n-BuLi and reactivity of n-BuLi. In our experiments, phase-pure orthorhombic Li_2SiO_3 NPs were produced with 1 : 3.75 molar equivalent of SiI_4 : n-BuLi whereas orthorhombic $Li_2Si_2O_5$ NPs were obtained with a slightly lower molar ratio of 1 : 2.25. In contrast, intermediate ratios of SiI_4 : n-BuLi consistently produced mixed phases of lithium silicates. Additionally, the reactivity of n-BuLi precursor has an effect on the crystal structure. It was also found that highly reactive n-BuLi (freshly prepared) can consistently produce Li_2SiO_3 NPs whereas less reactive n-BuLi (older than 2 weeks) tends to produce $Li_2Si_2O_5$ NPs. It is important to note that prior reports on lithium silicates point to orthorhombic crystal structure for Li_2SiO_3 (space group *Cmc21*)[51] whereas the crystal structure of $Li_2Si_2O_5$ is also orthorhombic (with *Ccc*2 space group),[52] although it is often referred to as monoclinic $Li_2Si_2O_5$.[8] In our calculations using PBE[18] parameterization of the GGA approximation[34] to the DFT, the unit cell of Li_2SiO_3 is orthorhombic with a=5.455 Å, b=9.476 Å, c=4.742 Å, which are close to experimental values of 5.397 Å, 9.392 Å, and 4.660 Å, respectively.[8] Likewise, for $Li_2Si_2O_5$ we obtain lattice constants of a=5.896 Å, b=14.797 Å, c=4.855 Å, while experimental values are 5.82 Å, 14.66 Å, and 4.79 Å, respectively.[8] Computed PBE relaxed crystal structures are shown in Figure 1, where each orthorhombic cell contains four formula units (vertical axis is along b lattice parameter), which are in agreement with the experimental diffraction patterns shown in Figure 2.

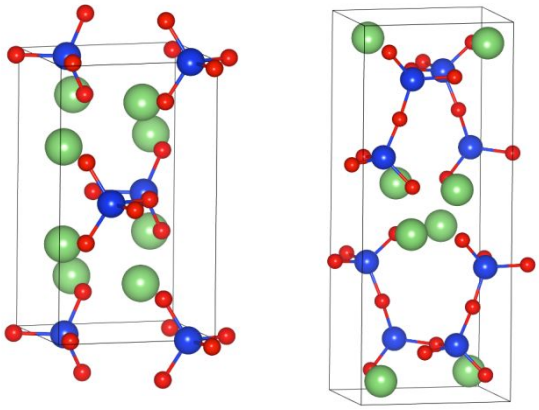

[A] Orthorhombic Li_2SiO_3; [space group: *Cmc21*]

[B] Orthorhombic $Li_2Si_2O_5$; [space group: *Ccc*2]

Figure 1. Unit cell structures of orthorhombic [A] Li_2SiO_3 and [B] $Li_2Si_2O_5$. The large green spheres are lithium, blue spheres are silicon, and small red spheres are oxygen.

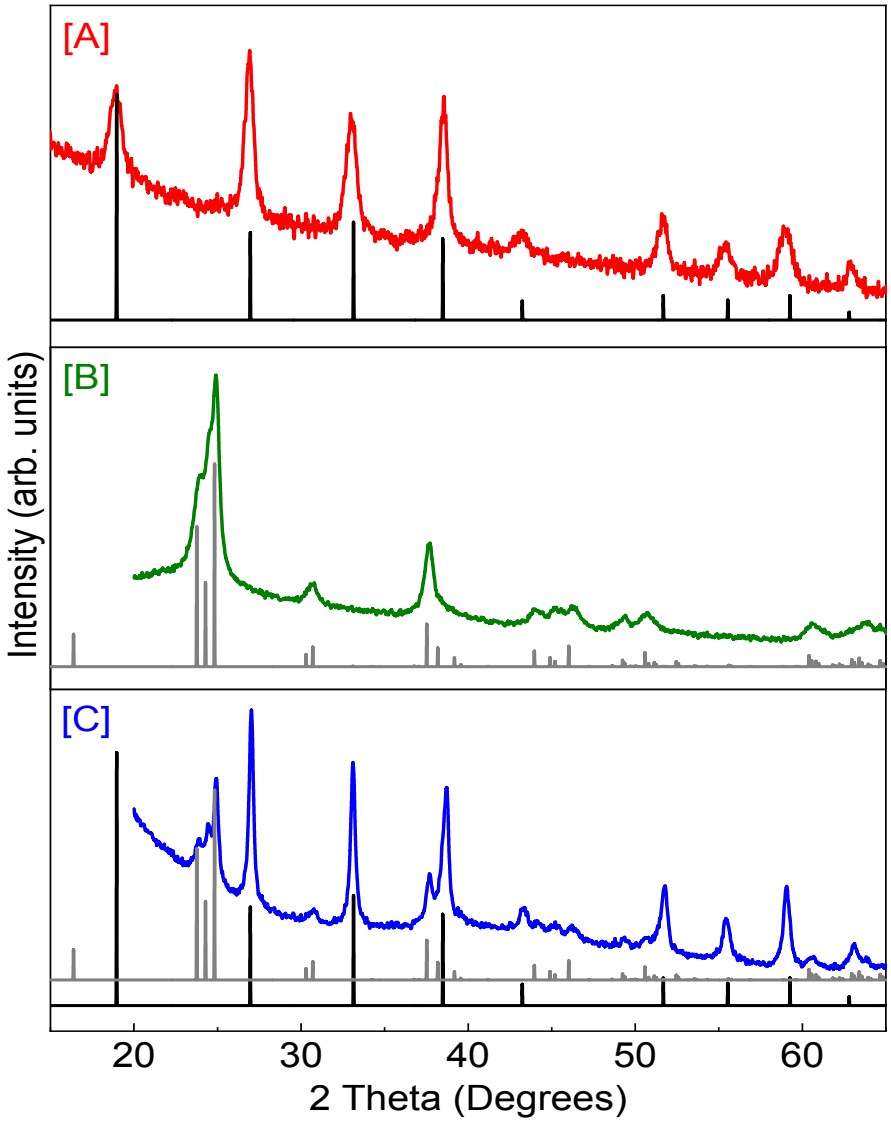

Figure 2. PXRD patterns of $Li_2Si_xO_y$ NPs annealed at 600 ºC: [A] orthorhombic Li_2SiO_3, [B] orthorhombic $Li_2Si_2O_5$, and [C] mixed phases of Li_2SiO_3 and $Li_2Si_2O_5$. Orthorhombic Li_2SiO_3 (JCPDS# 00-029-0829) and $Li_2Si_2O_5$ (JCPDS#01-070-4856) reference patterns are shown as vertical black and gray lines, respectively.

To corroborate with PXRD data, X-ray photoelectron spectra (XPS) were recorded to probe the chemical states of as-synthesized $Li_2Si_xO_y$, orthorhombic Li_2SiO_3 and $Li_2Si_2O_5$ NPs (Figure 3 and Supporting Information, Figure S2 and S3). Comparing the Li_2SiO_3 and $Li_2Si_2O_5$ chemical

formulae, one would expect more positive character of Si and Li in the latter, which would shift the binding energies to higher values. Oxygen, on the other hand, is expected to have a lower negative character for $Li_2Si_2O_5$ phase, which would shift corresponding binding energies to higher values. The examination of Si 2p spectra of orthorhombic Li_2SiO_3 NPs reveals two deconvoluted peaks at 101.62 and 102.96 eV, corresponding to Si-Si_2O_2 and Si-SiO_3 bonds, respectively.[53] In contrast, the deconvoluted Si 2p peaks of orthorhombic $Li_2Si_2O_5$ NPs exhibit higher binding energies of 103.20 and 103.62 eV, consistent with Si-O_4 and Si-O_2 bonds.[53,54] It is important to note that no peaks corresponding to Si^0 (binding energy of ~99.44 eV) were detected in any of the samples examined.

O 1s spectra of Li_2SiO_3 NPs exhibit binding energies of 529.70, 532.23, and 534.10 eV that can be attributed to different sub-oxides. Likewise $Li_2Si_2O_5$ NPs exhibit O 1s peaks at 530.70 and 532.90 eV, owing to different bonding environments of sub-oxides.[53, 54] The binding energy of Li 1s peak corresponding to Li-O bond (Li^+) is shifted from 55.04 eV in Li_2SiO_3 to 56.57 eV in $Li_2Si_2O_5$ NPs (Figure 3A-B), which can also be attributed to increased positive character of Li in the latter crystals.[55] To probe the differences in chemical states before and after annealing, XPS spectra of amorphous-to-poorly crystalline $Li_2Si_xO_y$ NPs were also recorded (Supporting Information, Figure S2). Both Si 2p and Li 1s binding energies of as-synthesized $Li_2Si_2O_5$ NPs are shifted to higher values compared to those of amorphous Li_2SiO_3 NPs (Supporting Information, Table S1), in agreement with their corresponding highly crystalline nanostructures (Figure 3A-B). These shifts are more pronounced in the annealed samples than in their as-synthesized counterparts likely due to increased crystallinity and long-range order.[54] Thus, it is likely that as-prepared poorly crystalline products of orthorhombic Li_2SiO_3 and $Li_2Si_2O_5$ NPs are internally different, which in turn lead to corresponding highly crystalline nanostructures.

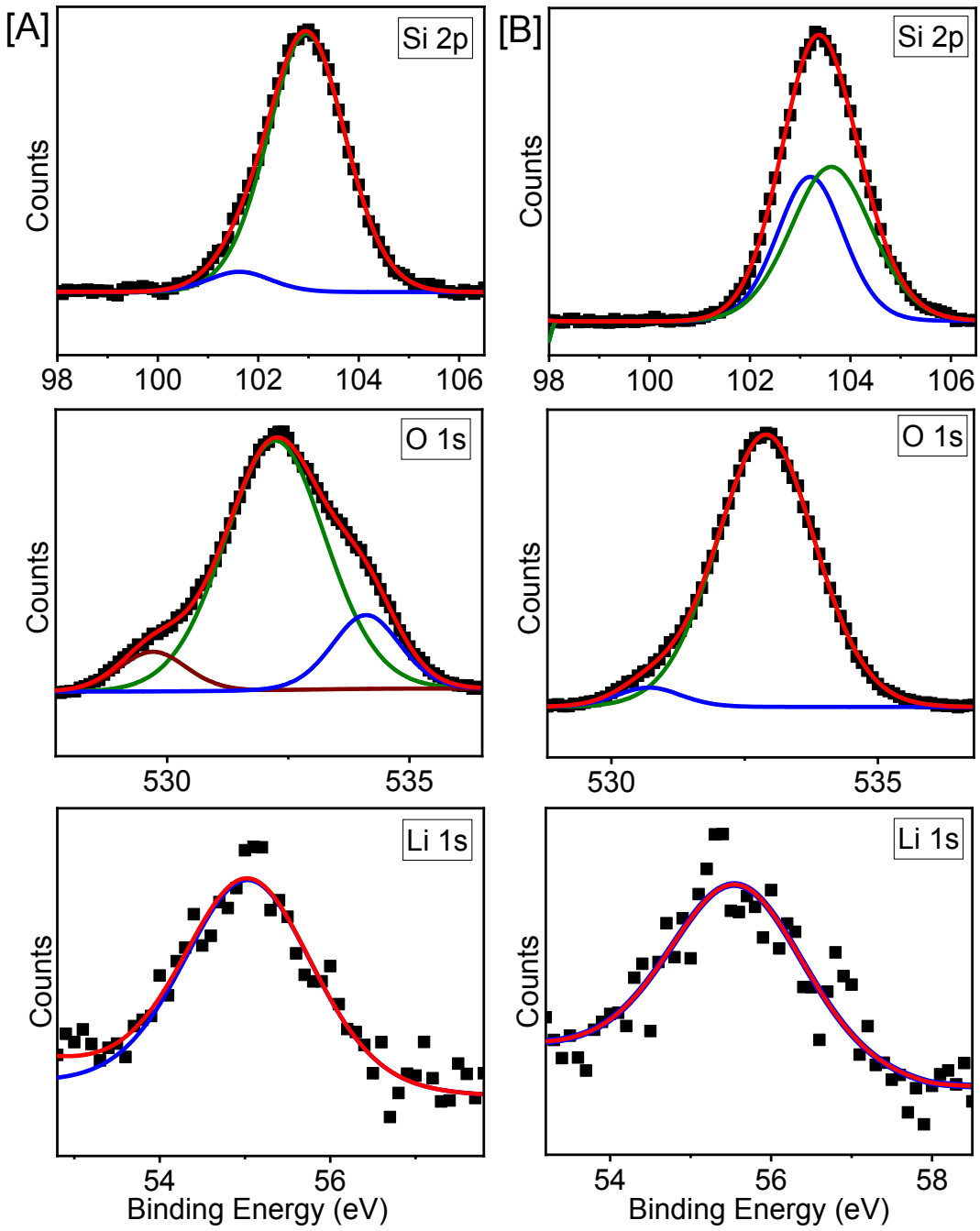

Figure 3. Si (2p), O (1s), and Li (1s) XPS spectra of phase-pure, orthorhombic (A) Li_2SiO_3 and (B) $Li_2Si_2O_5$ nanostructures produced via post-synthetic annealing of as-synthesized amorphous-to-poor crystalline $Li_2Si_xO_y$ NPs. Square symbols represent spectral data whereas the solid blue, green and wine lines are fitted deconvolutions. The red lines are spectral envelopes.

Low-resolution TEM images of amorphous-to-poorly crystalline Li_2SiO_3 NPs indicate spherical morphology and narrow size dispersity with average size of 8.7 ± 1.9 nm (Figure 4A and Supporting Information, Figure S4). Corresponding HRTEM images reveal the polycrystallinity of particles with a lattice spacing of 3.3 Å, which can be assigned to (111) plane of orthorhombic Li_2SiO_3 (Figure 4E). In contrast, as-synthesized $Li_2Si_2O_5$ NPs exhibit polyhedral morphology, a noteworthy increase in size dispersity (~2–15 nm), and a lattice spacing of 2.9 Å corresponding to (200) plane of orthorhombic $Li_2Si_2O_5$ (Figure 4B,F and Supporting Information, Figure S5). The HRTEM images show polycrystalline crystal arrangement in as-synthesized NPs, which is likely responsible for the amorphous moiety in corresponding diffraction patterns. In contrast, annealed orthorhombic silicates exhibit high crystallinity and a noteworthy increase in particle size owing to agglomeration/growth of NPs at elevated temperatures. Interestingly, annealed Li_2SiO_3 NPs show spherical crystals with ~10–700 nm diameter (Figure 4C and Supporting Information, Figure S6) whereas the annealed $Li_2Si_2O_5$ NPs show polyhedral or rod-shaped crystals (Figure 4D and Supporting Information, Figure S7) with ~5–80 nm. Corresponding HRTEM images indicate lattice spacing of 2.7 and 2.9 Å that can be assigned to (310) and (200) planes of orthorhombic Li_2SiO_3 and $Li_2Si_2O_5$, respectively (Figure 4G,H). It should be noted that annealed orthorhombic silicates were sonicated in $CHCl_3$ for TEM grid preparation, which presumably lead to breakup of the larger particles further increasing the size dispersity of annealed NPs.

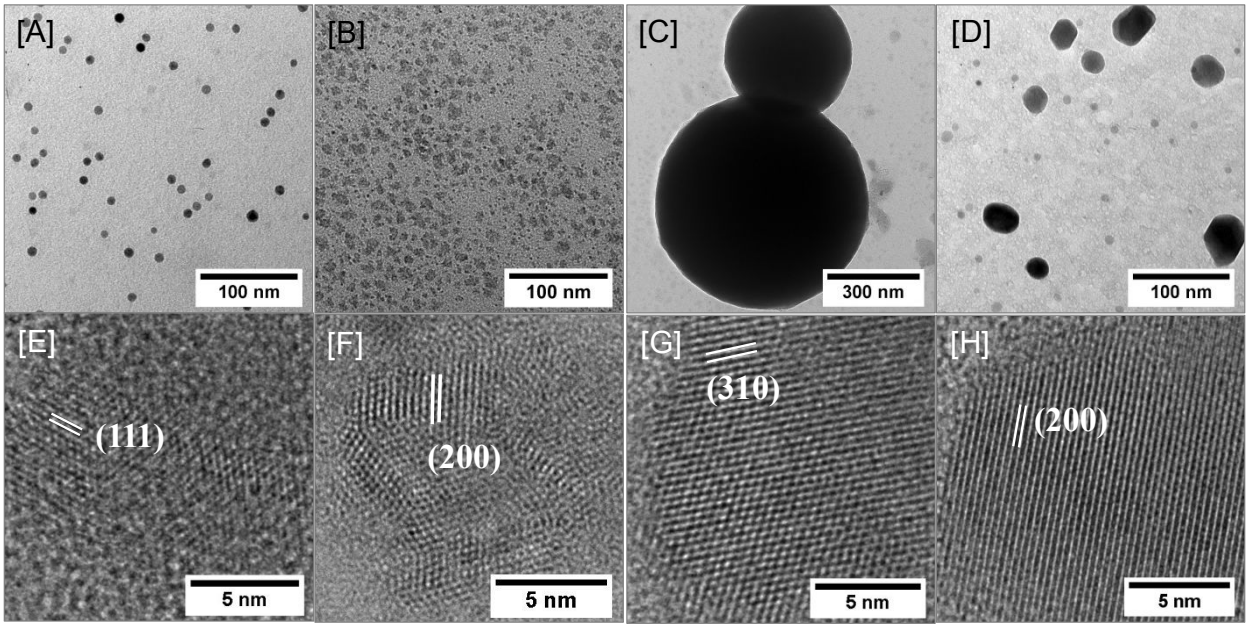

Figure 4. Low-resolution TEM and HRTEM images of as-synthesized, amorphous-to-poorly crystalline [A, E] Li_2SiO_3 and [B, F] $Li_2Si_2O_5$ NPs and their annealed orthorhombic [C, G] Li_2SiO_3 and [D, H] $Li_2Si_2O_5$ NP counterparts. HRTEM images show inter-planar distances of 3.3, 2.7, and 2.9 Å, which can be assigned to orthorhombic Li_2SiO_3 (111), orthorhombic Li_2SiO_3 (310) and orthorhombic $Li_2Si_2O_5$ (200) planes, respectively.

The surface characteristics of amorphous and crystalline lithium silicates were investigated using FT-IR spectroscopy (Figure 5). The IR spectra of amorphous-to-poorly crystalline $Li_2Si_xO_y$ NPs reveal the presence of stretching (ν) and bending (δ) vibrations of alkylamine and alkane surface ligands and Si-O bonds in the core of silicate particles: $\delta_{(Si\text{-}O)}$ at ~450 cm^{-1}, $\nu_{(Si\text{-}O\text{-}R)}$ at ~ 1000 cm^{-1}, $\nu_{(CHx)}$ at ~2850 cm^{-1}, $\delta_{(CH2)}$ at ~1500 cm^{-1}, $\nu_{(C=C)}$ at ~1600 cm^{-1}, and $\nu_{(Si\text{-}Si)}$ or $_{(Si\text{-}C)}$ at ~ 800 cm^{-1}.[2, 48] The CH_2, CH_x, and C=C vibrations are likely arise from surface bound oleylamine or butyl ligands whereas the Si-O and Si-O-R vibrations can be attributed to respective bonds in the polycrystalline core of silicate crystals (Figure 5a-b). Additionally, broad humps observed at

~3500 cm^{-1} further prove the presence of amine ligands coordinated to silicates. In contrast, annealed orthorhombic silicates show no peaks beyond 1300 cm^{-1} corresponding to amines or alkanes, consistent with the removal of surface ligands upon annealing at 600 ºC (Figure 5c-d).

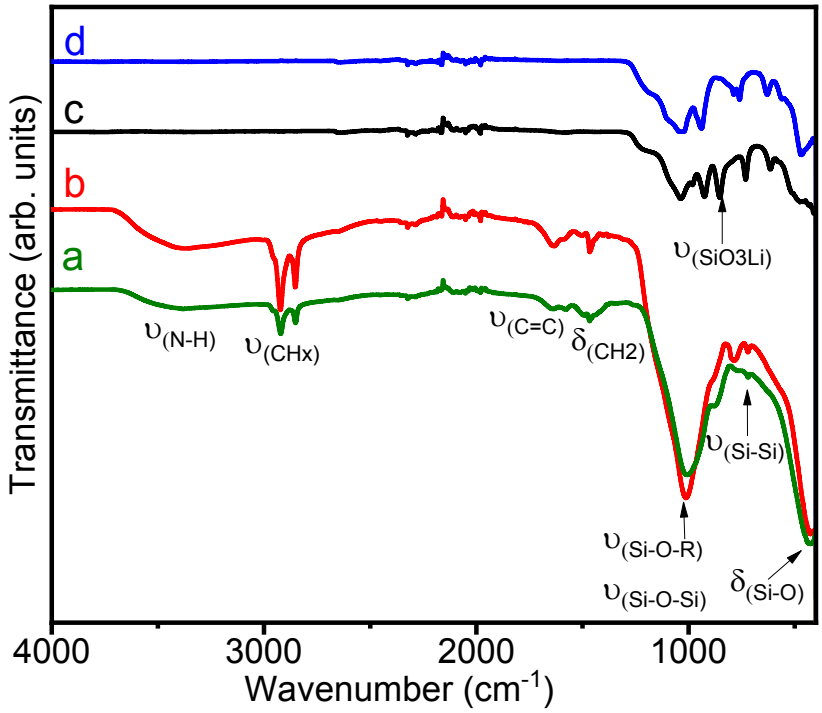

Figure 5. FT-IR spectra of as-synthesized (a) Li_2SiO_3 and (b) $Li_2Si_2O_5$ NPs along with annealed orthorhombic (c) Li_2SiO_3 and (d) $Li_2Si_2O_5$ NPs.

Colloidal solutions of amorphous-to-poorly crystalline $Li_2Si_xO_y$ NPs exhibit intense blue PL with a maximum at ~406 nm and a PLE maximum at ~315 nm (Figure 6A). The observed PL is independent of the size, shape, and crystal structure of silicate NPs as well as the excitation energy and therefore assumed to originate from emissive surface/interface states. Similar high intensity blue PL has also been reported for a number of wet-chemically produced Si and SiO_x crystals.[14, 56-58] Compared to solution state measurements, PL spectra of the solid-state samples exhibit a red shifted PL maximum at ~455 nm (Figure 6B), likely due to the partial removal of

surfactant ligands and subsequent resonant energy transfer between NPs in solid form.[59, 60] PL quantum yields of $Li_2Si_xO_y$ NPs dispersed in $CHCl_3$ were measured with respect to quinine sulfate and indicate values within 10–30%. The solid state TRPL spectra recorded at 15 K and 295 K show bi-exponential decays of 2.7–10.8 and 0.8–7 ns (Figure 6C-D and Table 1), as a result of different radiative and nonradiative decay pathways present in the system.[17, 58] The PL intensity at 295 K is approximately 1/10 of that at 15 K (Supporting Information, Figure S8), likely due to thermal activation of the nonradiative channels and subsequent reduction in surface emission.[56, 61] In addition, PL spectra recorded at 295 K are slightly blue-shifted compared to those recorded at 15 K. This temperature dependent blue-shifting has also been observed by Chandra *et al.*[58] for amorphous SiO_x NPs and attributed to enhanced interaction of electron-phonon scattering, which also enhances both radiative and nonradiative recombination rates. It has been reported that for luminescent SiO_x NPs, the surface/interface states created by carbon, nitrogen, and oxygen centers of the ligands can produce emissive traps that are likely responsible for the high intensity blue PL.[58, 62] In contrast, annealed orthorhombic Li_2SiO_3 and $Li_2Si_2O_5$ NPs show a noticeable decrease in PL intensity owing to removal of surface passivating ligands and creation of more nonradiative recombination channels. It is important to note that free surface ligands (OLA/HDD) and those reduced with n-BuLi at 250 ºC show weak PL peaks at 356 nm and 354 nm (Supporting Information, Figure S9), suggesting the necessity of silicate NPs to observe the high intensity visible PL.

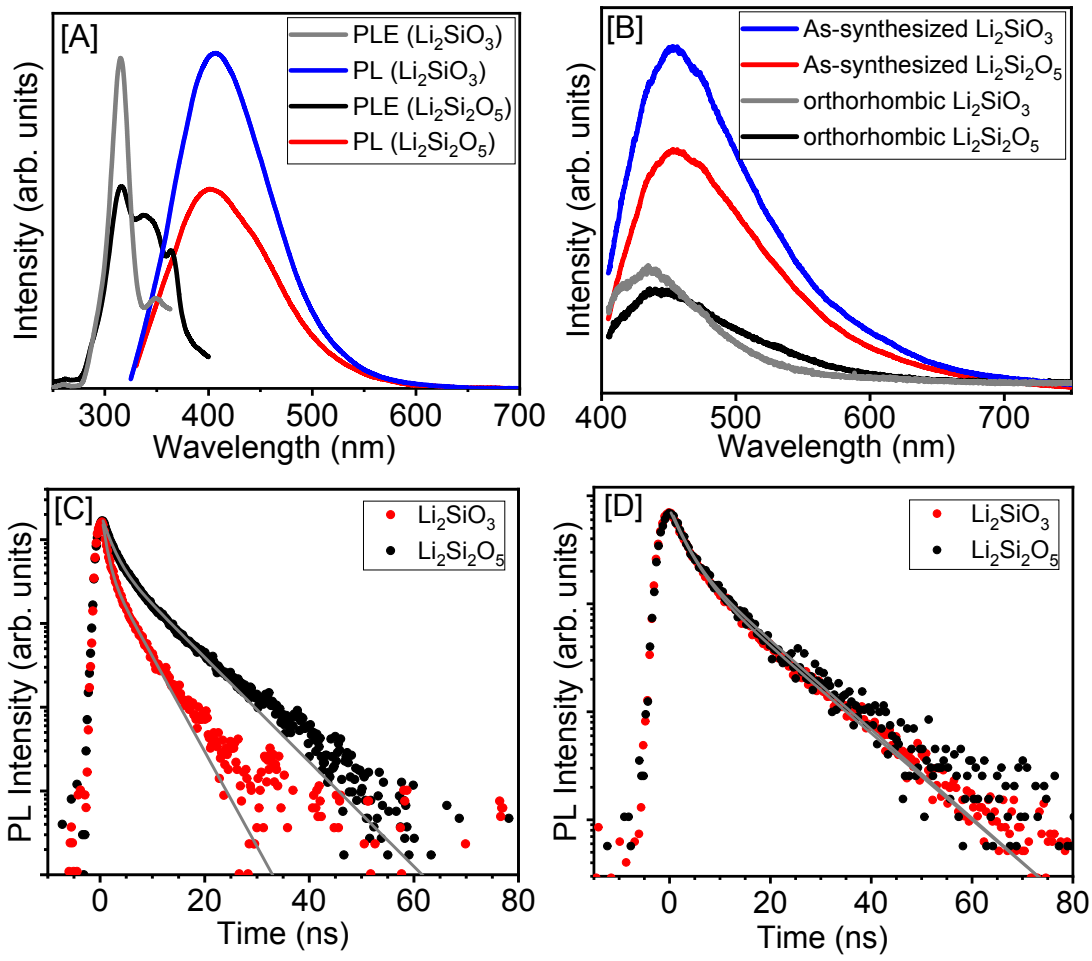

Figure 6. Room temperature [A] solution-state PL and PLE spectra of as-synthesized $Li_2Si_xO_y$ NPs. [B] Room temperature solid state PL spectra of as-synthesized $Li_2Si_xO_y$ NPs and annealed orthorhombic Li_2SiO_3 and $Li_2Si_2O_5$ NPs. [C] Room temperature (295 K) and [D] Low temperature (15 K) PL transients of as-synthesized Li_2SiO_3 and $Li_2Si_2O_5$ NPs. The dotted symbols are experimental data and the solid lines are biexponential fits.

Table 1. Time Constants Extracted from Biexponential Decay Fits ($A_{fast}\, e^{-t/\tau_{fast}} + A_{slow}\, e^{-t/\tau_{slow}}$) to PL Transients of As-Synthesized $Li_2Si_xO_y$ NPs.

@ 295 K	τ_{fast} **(ns)**	τ_{slow} **(ns)**	A_{fast} / A_{slow}
Li_2SiO_3	0.82 ± 0.01	3.83 ± 0.05	3.70
$Li_2Si_2O_5$	1.72 ± 0.02	6.96 ± 0.06	2.05
@ 15 K			
Li_2SiO_3	3.14 ± 0.05	10.83 ± 0.19	1.94
$Li_2Si_2O_5$	2.70 ± 0.09	10.56 ± 0.26	1.63

Solid-state absorption spectra of as-synthesized Li_2SiO_3 and $Li_2Si_2O_5$ NPs show the lowest energy absorption onsets at 3.47 and 3.49 eV, respectively (Figure 7). Additionally, well-defined absorption onsets were also noted at 5.11 eV and 5.29 eV, respectively. Literature reports on lithium silicates suggest controversial values for energy gaps from 4.48–7.45 eV for bulk orthorhombic Li_2SiO_3 and $Li_2Si_2O_5$.[19, 21, 22, 25, 63] Thus, to accurately correlate our absorption measurements with optical transitions, HSE calculations were performed to determine the bulk bandgaps of orthorhombic Li_2SiO_3 and $Li_2Si_2O_5$. Figure 7 shows the calculated absorption spectra of Li_2SiO_3 and $Li_2Si_2O_5$ using TD-HSE theory, which includes electron-hole interactions. In both materials, theoretically predicted absorption onsets (~7.8 eV) are significantly larger than the values obtained in experiments. This discrepancy seems unusual because theoretical DFT based methods (including hybrid functionals) tend to underestimate the bandgaps of insulators and semiconductors. Therefore, to further elucidate the difference between experimental and theoretical absorption spectra, the underlying electronic structure was examined.

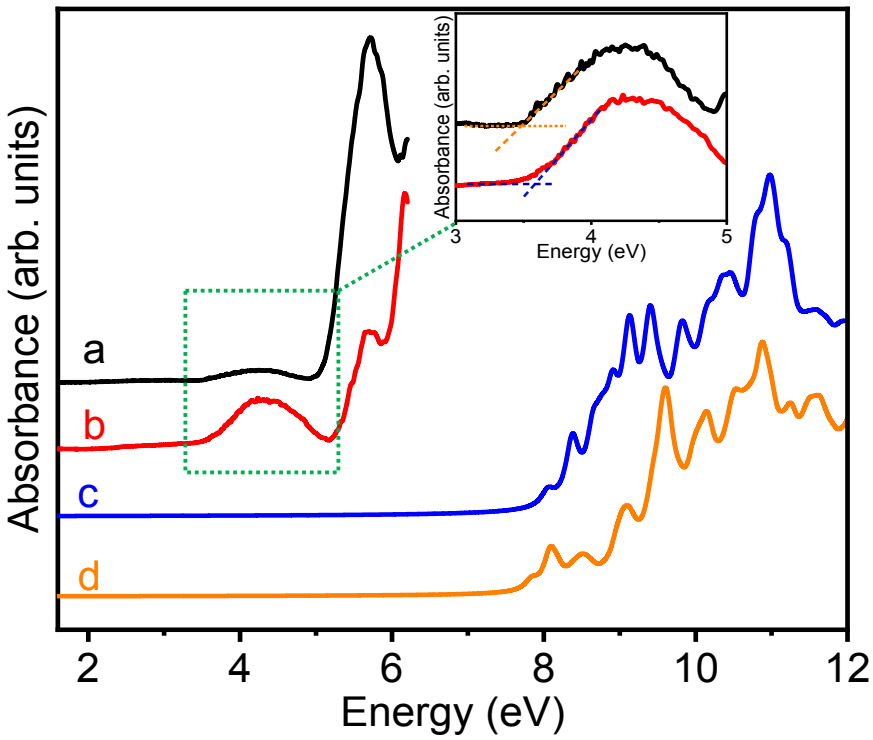

Figure 7. Solid-state absorption spectra of as-synthesized (a) Li_2SiO_3 and (b) $Li_2Si_2O_5$ NPs along with absorption spectra calculated using TD-HSE for orthorhombic (c) Li_2SiO_3 and (d) $Li_2Si_2O_5$.

HSE band structure calculations of bulk Li_2SiO_3 and $Li_2Si_2O_5$ were performed on PBE relaxed lattice structures (Supporting Information, Figure S10). The **k**-point path for orthorhombic structures was chosen as described in Setyawan et al.[54] The band structures of the two materials are very similar, with energy gaps of ~7.8 eV for both materials. The only significant difference is the nature of the bandgap, where Li_2SiO_3 exhibits an indirect Γ-Z bandgap, while $Li_2Si_2O_5$ exhibits a direct bandgap. In either case, as expected, the HSE computed bandgaps are significantly larger than those previously obtained with semi/local approximations to the DFT.[8, 19, 21] This is typical for extended solids, where HSE significantly improves the computed electronic structure. These results suggest that the PL observed below

7.8 eV for Li_2SiO_3 and $Li_2Si_2O_5$ NPs is most likely originating from the surface states or other defect states and not from the inter-band electronic transitions. Amorphous solids are expected to exhibit reduced bandgaps compared to bulk crystalline structures used in our calculations. However, the differences between theoretical bandgaps and measured absorption onsets and PL spectra are far too large to be explained by tails of densities of states due to an amorphous structure. Thus, the measured absorption onsets and PL do not represent energy gaps of Li_2SiO_3 and $Li_2Si_2O_5$ NPs, but rather transitions via defect or surface states below the bandgap. It should also be noted that the transition energies will be even higher when size confinement effects are considered for NPs of size smaller than the exciton Bohr radius.

CONCLUSIONS

We have successfully produced lithium metasilicate and disilicate nanostructures with spherical, polyhedral to rod morphology and two distinct crystal structures via a facile low temperature colloidal chemistry method. As-synthesized NPs show poor crystallinity, which after annealing at 600 °C produced phase-pure orthorhombic Li_2SiO_3 and $Li_2Si_2O_5$ nanostructures. It should be noted that a similar synthetic strategy has been claimed to produce a new exotic phase of Si NPs (BC8 structure type).[13] The amorphous and orthorhombic Li_2SiO_3 and $Li_2Si_2O_5$ NPs exhibit substantial differences in internal chemical structures as probed by XPS. The Li and Si binding energies of $Li_2Si_2O_5$ NPs are significantly higher than those of the Li_2SiO_3 NPs, owing to increased positive character of constituent elements in $Li_2Si_2O_5$ NPs. Interestingly, the as-prepared counterparts of orthorhombic Li_2SiO_3 and $Li_2Si_2O_5$ NPs (*i.e.* $Li_2Si_xO_y$ NPs) exhibit similar binding energies indicating that corresponding crystal structures are formed during the synthesis and the post-synthetic annealing step provided the complimentary energy to improve the crystallinity of $Li_2Si_xO_y$ NPs. The surface of the as-

synthesized $Li_2Si_xO_y$ NPs is passivated with oleylamine and alkyl ligands, which completely decompose upon annealing and only Si-O and Si-O-R species of the core material are present in annealed orthorhombic Li_2SiO_3 and $Li_2Si_2O_5$ NPs. Similar to Si QDs with diamond cubic and BC8 structure types, as-synthesized $Li_2Si_xO_y$ NPs exhibit high intensity blue PL, which we attribute to surface/interface defects. Exchange tuned HSE hybrid functional calculations preformed on orthorhombic Li_2SiO_3 and $Li_2Si_2O_5$ bulk crystals reveal indirect and direct energy gaps of 7.79 and 7.80 eV, respectively. With quantum confinement effects transition energies are expected to be even higher for orthorhombic Li_2SiO_3 and $Li_2Si_2O_5$ NPs, which were not probed due to instrument limitations.

ELECTRONIC SUPPLEMENTRY INFORMATION

The Electronic Supplementary Information (ESI) is available: Powder X-ray diffraction pattern and XPS survey scan of as-synthesized $Li_2Si_xO_y$ NPs; Li (1s), O (1s), and Si (2p) XPS spectra and corresponding binding energies of as-synthesized $Li_2Si_xO_y$ NPs; TEM images of as-synthesized $Li_2Si_xO_y$ NPs along with orthorhombic Li_2SiO_3 and $Li_2Si_2O_5$ NPs; and solid-state PL spectra of Li_2SiO_3 and $Li_2Si_2O_5$ NPs.

Corresponding Author

*Indika U. Arachchige; E-mail: iuarachchige@vcu.edu

Conflicts of interest

There are no conflicts of interest to declare.

ACKNOWLEDGMENTS

Authors acknowledge Dr. Liu for the assistance with HRTEM analysis at North Carolina State University, which is supported by the State of North Carolina and the National

Science Foundation. Theoretical part of this work was supported by the VCU Center for High Performance Computing. Authors gratefully acknowledge the U.S. National Science Foundation (DMR-1506595) for financial support. E.H.E. acknowledges Egyptian government for her doctoral scholarship.

REFERENCES

1. O. Namur and B. Charlier, *Nat. Geosci.*, 2017, **10**, 9–13.
2. A. Nakagawa, N. Kuwata, Y. Matsuda and J. Kawamura, *J. Phys. Soc. Jpn.*, 2010, **79**, 98-101.
3. S.-i. Furusawa, A. Kamiyama and T. Tsuruib, *Solid State Ionics*, 2008, **179**, 536–542.
4. S. Furusawa, T. Kasahara and A. Kamiyama, *Solid State Ionics*, 2009, **180**, 649-653.
5. O. V. Savvova, L. L. Bragina, D. V. Petrov, V. L. Topchii and S. A. Ryabinin, *Glass Ceram.*, 2018, **4**, 3-9.
6. D. Cruz, S. Bulbulian, E. Lima and H. Pfeiffer, *J. Solid State Chem.*, 2006, **179**, 909-916.
7. K. B. Saad, H. Hamzaoui, A. Labidi and B. Bessaïs, *Appl. Surf. Sci.*, 2008, **254**, 3955-3958.
8. Y. Duan, H. Pfeiffer, B. Li, I. C. Romero-Ibarra, D. C. Sorescu, D. R. Luebke and J. W. Halley, *Phys. Chem. Chem. Phys.*, 2013, **15**, 13538-13558.
9. P. V. Subha, B. N. Nair, P. Hareesh, A. P. Mohamed, T. Yamaguchi, K. G. K. Warrier and U. S. Hareesh, *J. Mater. Chem. A*, 2014, **2**, 12792–12798.
10. J.-H. Ahn, Y.-J. Kim and G. Wang, *Nanoscale Res. Lett.* , 2010, **5**, 1841-1845.

11. J. Hmäläinen, F. Munnik, T. Hatanpää, J. Holopainen, M. Ritala and M. Leskelä, *J. Vac. Sci. Technol. A*, 2012, **30**, 01A106/101-101A106/105.

12. Q. Sun, B. Zhang and Z.-W. Fu, *Appl. Surf. Sci.* , 2008, **254**, 3774-3779.

13. S. Ganguly, N. Kazem, D. Carter and S. M. Kauzlarich, *J. Am. Chem. Soc.* , 2014, **136**, 1296−1299.

14. D. E. Harwell, J. C. Croney, y. W. Qin, J. T. Thornton, J. H. Day, E. K. Hajime and D. M. Jameson, *Chem. Lett.*, 2003, **32**, 1194-1195.

15. D. Neiner, H. W. Chiu and S. M. Kauzlarich, *J. Am. Chem. Soc.*, 2002, **128**, 11016-11017.

16. X. Cheng, R. Gondosiswanto, S. Ciampi, P. J. Reeceb and J. J. Gooding, *Chem. Commun.*, 2012, **48**, 11874–11876.

17. K. i. Dohnalova´, A. N. Poddubny, A. A. Prokofiev, W. D. d. Boer, C. P. Umesh, J. M. Paulusse, H. Zuilhof and T. Gregorkiewicz, *Light: Sci. Appl.*, 2013, **2**, 1-6.

18. J. P. Perdew, K. Burke and M. Ernzerhof, *Phys. Rev. Lett.*, 1996, **77**, 3865-3868.

19. A. Alemi, S. Khademinia, S. W. Joo, M. Dolatyari and A. Bakhtiari, *Int. Nano Lett.*, 2013, **3**, 1-11.

20. J. P. Perdew and Y. Wang, *Phys. Rev. B*, 1992, **45**, 13244-13249.

21. J. Du and L. R. Corrales, *J. Phys. Chem. B*, 2006, **110**, 22346-22352.

22. W. Y. Ching, Y. P. Li, B. W. Veal and D. J. Lam, *Phy. Rev. B*, 1985, **32**, 1203-1207.

23. A. Yang, H. Wang, W. Li and J. Shi, *J. Am. Ceram. Soc.*, 2012, **95**, 1818-1821.

24. A. Chen and P. F. James, *J. Non-Cryst. Solids*, 1988, **100**, 353-358.

25. A. Alemi and S. Khademinia, *Int. Nano Lett.*, 2015, **5**, 15-20.

26. A. Alemi, S. Khademinia, M. Dolatyari and A. Bakhtiari, *Int. Nano Lett.*, 2012, **2**, 1-9.

27. D. Zhang, X. Pu, S. I. Kim, P. Cai, C. Chen and H. J. Seo, *J. Lumin.*, 2015, **168**, 293-296.

28. S. Lou, T. Xuan, Q. Liang, J. Huang, L. Cao, C. Yu, M. Cao, C. Xia, J. Wang, D. Zhang and H. Li, *J. Colloid Interface Sci.*, 2019, **537**, 384–388.

29. C. Xia, C. Yu, M. Cao, J. Xia, D. Jiang, G. Zhou, D. Zhang and H. Li, *Ceram. Int.*, 2018, **44**, 21040–21046.

30. M. Nowak, B. Kauch and P. Szperlich, *Rev. Sci. Instrum.*, 2009, **80**, 046107/046101-046107/046103.

31. J. Zhang, Y. Yang, H. Deng, U. Farooq, X. Yang, J. Khan, J. Tang and H. Song, *ACS Nano*, 2017, **11**, 9294−9302.

32. G. Kresse and J. Furthmüller, *Phys. Rev. B*, 1996, **54**, 11169-11186.

33. P. E. Blöchl, *Phys. Rev. B*, 1994, **50**, 17953-17979.

34. J. P. Perdew, *Phys. Rev. Lett.*, 1985, **55**, 1665-1668.

35. J. Heyd, G. E. Scuseria and M. Ernzerhof, *J. Chem. Phys.*, 2003, **118**, 8207-8215.

36. M. Marsman, J. Paier, A. Stroppa and G. Kresse, *J. Phys.: Condens. Matter.*, 2008, **20**, 1-9.

37. M. Toporkov, D. O. Demchenko, Z. Zolnai, J. Volk, V. Avrutin, H. Morkoç and U. Özgür, *J. Appl. Phys.*, 2016, **119**, 095311/095311-095311/095319.

38. Z. Zolnaia, M. Toporkov, J. Volka, D. O. Demchenko, S. Okur, Z. Szabó, U. Özgür, H. Morkoc, V. Avrutin and E. Kótai, *Appl. Surf. Sci.*, 2015, **327**, 43-50.

39. J. Paier, M. Marsman and G. Kresse, *Phys. Rev. B*, 2008, **78**, 121201-121201/121201-121204

40. M. E. Casida, *Journal*, 1995, **1**.

41. C. Banerjee, C. R. Wade, A. Soulet, G. Jursich, J. McAndrew and J. A. Belot, *Inorg. Chem. Commun.*, 2006, **9**, 761–763.

42. R. J. A. Esteves, S. Hafiz, D. O. Demchenko, Ü. Özgür and I. U. Arachchige, *Chem. Commun.*, 2016, **52**, 11665-11668.

43. R. J. A. Esteves, M. Q. Ho and I. U. Arachchige, *Chem. Mater.*, 2015, **27**, 1559–1568.

44. D. C. Lee, J. M. Pietryga, I. Robel, D. J. Werder, R. D. Schaller and V. I. Klimov, *J. Am. Chem. Soc.*, 2009, **131**, 3436–3437.

45. K. Ramasamy, P. G. Kotula, A. F. Fidler, M. T. Brumbach, J. M. Pietryga and S. A. Ivanov, *Chem. Mater.*, 2015, **27**, 4640-4649.

46. M. T. Swihart, *Nanotechnology in Biology and Medicine: Methods, Devices, and Applications*, Taylor and Francis Group, LLC, 2006 edn., 2007.

47. R. K. Baldwin, K. A. Pettigrew, J. C. Garno, P. P. Power, G.-y. Liu and S. M. Kauzlarich, *J. Am. Chem. Soc.*, 2002, **124**, 1150-1151.

48. C.-S. Yang, R. A. Bley, S. M. Kauzlarich, H. W. H. Lee and G. R. Delgado, *J. Am. Chem. Soc.* , 1999, **121**, 5191-5195.

49. S. Jang, J. Kim, Y. Koh, K. Jung, H.-G. Woo and H. Sohn, *J. Nanosci. Nanotechnol.*, 2010, **10**, 3557–3561.

50. H. Gilman, R. A. Benkeser and G. E. Dunn, *J. Am. Chem. Soc.*, 1950, **72**, 1689–1691.

51. K. Persson, 2014, DOI: 10.17188/1208560.

52. K. Persson, 2016, DOI: 10.17188/1207865.

53. T. P. Nguyen and S. Lefrant, *J. Phys.: Condens. Matter.*, 1989, **1**, 5197-5204.

54. A. Cros, R. Saoudi, G. Hollinger, C. A. Hewett and S. S. Lau, *J. Appl. Phys.*, 1990, **67**, 1826-1830.

55. T. M. Grehk, L. S. O. Johansson, S. M. Cray, M. Johansson and A. S. Flodström, *Phys. Rev. B*, 1995, **52**, 16593-16601.

56. Q. Li, T.-Y. Luo, M. Zhou, H. Abroshan, J. Huang, H. J. Kim, N. L. Rosi, Z. Shao and R. Jin, *ACS Nano*, 2016, **10**, 8385−8393.

57. E. V. Rogozhina, D. A. Eckhoff, E. Gratton and P. V. Braun, *J. Mater. Chem.*, 2006, **16**, 1421–1430.

58. S. Chandra, G. g. Beaune, N. Shirahata and F. M. Winnik, *J. Mater. Chem. B*, 2017, **5**, 1363-1370.

59. Z. Lin, H. Li, A. Franceschetti and M. T. Lusk, *ACS Nano*, 2012, **VOL. 6**, 4029–4038.

60. S. W. Clark, J. M. Harbold and F. W. Wise, *J. Phys. Chem. C* 2007 **111**, 7302-7305.

61. D. Gerion, N. Zaitseva, C. Saw, M. F. Casula, S. Fakra, T. V. Buuren and G. Galli, *Nano Lett.*, 2004, **4**, 597-602.

62. A. Puzder, A. J. Williamson, J. C. Grossman and G. Galli, *J. Chem. Phys.*, 2002, **117**, 6721-6729.

63. T. Tang and D.-L. Luo, *J. At. Mol. Sci.*, 2010, **1**, 185-200.

TOC image

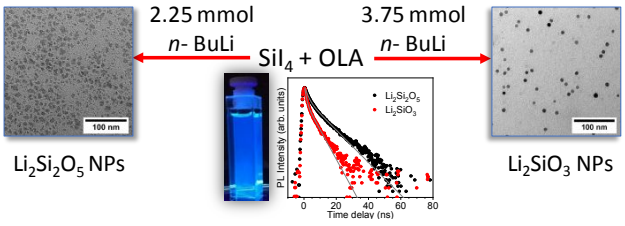

Colloidal synthesis of lithium silicate nanocrystals with varying morphology, composition, crystal structure, and high intensity visible luminescence is reported.